Check for updates

Spatial scale dependence of the relationship between turbulent surface heat flux and SST

Xiaoshan Sun[1,3] · Renguang Wu[1,2,4]

Abstract

This study investigates the spatial scale dependence of relationship between turbulent surface heat flux (SHF) and sea surface temperature (SST) variations in the mid-latitude frontal zones, subtropical gyres, and tropical Indo-western Pacific region in winter and summer with daily observational data. A comparison of the SHF and SST/SST tendency correlation between 1° and 4° spatial scale displays a decrease of the positive SHF–SST correlation and an increase of the negative SHF–SST tendency correlation as the spatial scale increases in all the above regions. The lead–lag SHF and SST/SST tendency correlation at different spatial scales illustrates an obvious transition from the oceanic forcing to the atmospheric forcing in the western boundary currents (WBCs) and the Agulhas Return Current (ARC) in both winter and summer. The transition length scale is smaller in summer than in winter, around 2.6°–4.5° in winter and around 0.8°–1.3° in summer based on the OAFlux data. In the subtropical gyres and tropical Indo-western Pacific region, atmospheric forcing dominates up to 10° spatial scale with the magnitude of forcing increasing with the spatial scale in both winter and summer except for the Arabian Sea in summer. The Arabian Sea distinguishes from the other tropical regions in that the SST forcing dominates up to more than 10° spatial scale in summer with the magnitude of forcing decreasing slowly with the spatial scale increase.

Keywords Surface heat flux–SST relationship · Spatial scale dependence · Seasonal difference · The mid-latitude frontal zones · The tropical Indo-western Pacific

1 Introduction

Ocean and atmosphere interacts closely with each other. As the largest underlying surface of the atmosphere, the ocean absorbs large amount of solar energy and releases most of the energy to the atmosphere to drive the atmospheric variability. In turn, the atmosphere modulates the thermal condition of the ocean by changes in wind, humidity and temperature. Compared to the atmosphere-only models, the ocean-atmosphere coupled models produce more realistic simulations due to the inclusion of coupled ocean-atmosphere processes (Manabe and Stouffer 1996; Barsugli and Battisti 1998; Kitoh and Arakawa 1999; Wu and Kirtman 2004, 2005, 2007; Wang et al. 2005; Wu et al. 2006; Fu et al. 2013).

Simultaneous correlation between sea surface temperature (SST) and turbulent surface heat flux (SHF) or precipitation has been used to document the relationship between ocean and atmosphere (Trenberth and Shea 2005; Wu and Kirtman 2005, 2007; Wu et al. 2007; Small et al. 2019). With a positive value denoting upward SHF, a positive correlation between SST and SHF is considered as the oceanic forcing of the atmosphere. In that case, the disequilibrium of temperature and humidity between the ocean and atmosphere causes sensible and latent heat loss from the ocean surface. In contrast, a negative correlation between the SST tendency (the difference of the succeeding SST minus the preceding SST in a time series divided by 2) and SHF indicates that the heat loss from the ocean surface contributes to the SST decrease, which

✉ Renguang Wu
renguang@zju.edu.cn

[1] Center for Monsoon System Research, Institute of Atmospheric Physics, Chinese Academy of Sciences, Beijing, China

[2] School of Earth Sciences, Zhejiang University, Hangzhou 310027, China

[3] College of Earth and Planetary Sciences, University of Chinese Academy of Sciences, Beijing, China

[4] Southern Marine Science and Engineering Guangdong Laboratory (Zhuhai), Zhuhai, China

is a signal of the atmospheric forcing of the ocean. In addition, the lead–lag correlation between SHF and SST, which shows detailed temporal relationship of the relevant atmospheric and oceanic changes, is another way to diagnose the relative importance of oceanic and atmospheric forcing (Frankignoul and Hasselmann 1977; Cayan 1992; Barsugli and Battisti 1998; Storch 2000; Wang et al. 2005; Wu et al. 2015; Wu and You 2018; Wu 2019; Sun and Wu 2021). The oceanic forcing is detected when the SHF–SST correlation is large positive at zero lag with an asymmetric structure of the lead–lag SHF–SST tendency correlation. If the simultaneous SHF–SST tendency correlation is large negative and the lead–lag SHF–SST correlation is symmetric, the atmospheric forcing is primary. The distinct relationship between the oceanic and atmospheric forcing cases has been demonstrated by a simple ocean-atmosphere energy balance model (Barsugli and Battisti 1998; Wu et al. 2006; Bishop et al. 2017).

The relationship between SST and SHF variations changes with temporal and spatial scales (Wu et al. 2015; Bishop et al. 2017; Small et al. 2019; Sun and Wu 2021) examined the changes of SST and SHF relationship with temporal scales using daily data and identified several transitions between the atmospheric and oceanic forcing at submonthly time scales that cannot be resolved based on monthly data. They also revealed seasonal differences of the temporal scale dependence of the SST and SHF relationship. The spatial scale dependence of the SST and SHF relationship and its seasonal difference has not been examined using daily data, which is the main thrust for the present study.

Studies have shown the relevance of the spatial resolution in the relationship between SST and SHF variations to the characteristics of ocean-atmosphere interactions. Kirtman et al. (2012) showed that the NCAR Community Climate System Model (CCSM) with a high spatial resolution exhibits stronger oceanic forcing to the atmosphere compared to the low spatial resolution model in the extratropics. Putrasahan et al. (2017) indicated that the global climate model with 0.1° ocean resolution largely reduces the bias of SHF–SST correlation in the Gulf of Mexico compared to the simulation of 1° ocean resolution. Small et al. (2019) compared simultaneous SHF–SST correlation among J-OFURO3 with 0.25° ocean resolution, Community Earth System Model-High Ocean Resolution (CESM-HR) with nominal 0.1° ocean resolution, and CESM-Low Ocean Resolution (CESM-LR) with 1° ocean resolution and found that the global spatial pattern of the correlation is much similar to that in the observations in CESM-HR than in CESM-LR. Bellucci et al. (2021) showed that the increase of ocean model resolution improves the representation of SHF and SST cross-covariance patterns. These previous studies indicate that the actual relationship between ocean and atmosphere can only be resolved with high spatial resolutions.

The spatial scale dependence of the ocean-atmosphere relationship is related to the presence of meso-scale SST fronts and the role of small scale ocean eddies. Small scale ocean eddies and meso-scale SST fronts have a great influence on the SHF change and play a prominent role in the air–sea relationship (Chelton et al. 2004; Small et al. 2008; Bryan et al. 2010; Chelton and Xie 2010). In those frontal SST regions, the ocean advection induced by ocean eddies acting on meso-scale SST gradients, if the spatial scale is small enough to resolve them, contributes to the SST changes notably, leading to the ocean-driven mode. In contrast, the low spatial resolution may reduce the SST gradients, leading to a weak oceanic forcing. In the western boundary currents (WBCs) and Agulhas Return Current (ARC), the high-speed ocean currents bring large amount of warm water from the low-latitude regions to the mid-latitude regions. The strong temperature advection changes the underlying surface of the atmosphere and causes heat loss from the ocean so that SHF is mainly driven by SST (Bishop et al. 2017; Small et al. 2019). In the subtropical gyres, the ocean currents are much weaker than the western boundaries and the SST gradients are small, and thus the SST change is mainly driven by SHF (Wu and Kinter 2010).

The change of the SHF and SST relationship with the spatial scale has been investigated by applying spatial smoothing (Bishop et al. 2017; Small et al. 2019). A transition length scale was defined by Bishop et al. (2017) to determine at which spatial scale the air–sea relationship changes. In the WBC regions, the transition from the SST forcing to the atmospheric forcing is at about 1°–4° length scale based on the OAFlux data. Small et al. (2019) did similar work using the J-OFURO3 and CESM-HR data and obtained 4°–7° length scales for the transition from the SST forcing to the atmospheric forcing and they speculated that the difference of result from Bishop et al. (2017) is due to the higher spatial resolution of updated data. In the subtropical gyre regions, the atmospheric forcing dominants at all the spatial scales (Bishop et al. 2017). Thus, the spatial scale dependence of the SHF and SST relationship varies with the region. The regional feature of the SHF and SST relationship may also be related to the spatial change of the high frequency atmospheric variance. In regions with large high frequency atmospheric activities, the atmosphere likely has a larger influence on the SST change (Wu et al. 2015; Wu and Chen 2015; Wu 2016).

The analysis of Bishop et al. (2017) and Small et al. (2019) about the spatial scale dependence of the SHF and SST relationship is based on monthly mean data. Submonthly variations have been identified in both the atmosphere and ocean. The submonthly time scale current structures can have an imprint on SHF (Wallace et al. 1990). The submonthly warm mesoscale heat flux convergence leads to the lateral advection and the SST anomalies have a close

relationship with SHF in the northwest part of anticyclonic Loop Current (LC) meanders in the Gulf of Mexico (Putrasahan et al. 2017), while the LC frontal eddies also display variations on submonthly time scales (Donohue et al. 2016; Jouanno et al. 2016). The time smoothing may eliminate the atmospheric high frequency noises that contributes to the low frequency variability of the ocean surface (Frankignoul and Hasselmann 1977; Hasselmann 1976; Deser and Timlin 1997; Frankignoul et al. 1998). When using monthly data, both oceanic forcing and atmospheric forcing can be included in the calculation of the correlation coefficient as the atmosphere responds to the SST anomalies quickly (within a week) and the ocean mixed layer can also react to the changing atmosphere in days to months (Wallace et al. 1990; Deser and Timlin 1997). Consequently, the spatial scale dependence of the SHF and SST relationship in various regions needs to be inspected using daily observational data to gain a better understanding of local air–sea interaction in short time scales. Apart from regional features, seasonal variations in the SHF and SST relationship have been identified in previous studies (Kushnir and Held 1996; Frankignoul et al. 1998; Wu and Kirtman 2005; Wu and Kinter 2010; Duvel and Viallard 2007; Putrasahan et al. 2013; Wu et al. 2015; Jing et al. 2020). Thus, it is necessary to examine the spatial scale dependence of the correlation between SHF and SST variations in different seasons.

This study investigates changes in the relationship between SST and SHF variations with the spatial scale in both winter and summer in the mid-latitude SST frontal zones, the subtropical gyres, and the tropical Indo-western Pacific region. The remaining part of the paper is organized in the following way. Section 2 introduces the datasets and methods used in this study. The conceptual stochastic climate model simulation results are shown in Sect. 3. In Sect. 4, the regional correlation is compared for 1° and 4° spatial scales. In Sect. 5, we present the spatial scale dependence of lead–lag correlation at selected locations in winter and summer. Section 6 focuses on the comparison of the transition length scale between winter and summer. Section 7 gives the summary and discussions.

2 Datasets and methods

For the daily observational SST data, we use the National Oceanic and Atmospheric Administration (NOAA) Optimum Interpolation Sea Surface Temperature (OISST) v2.0 (Reynolds et al. 2007). This dataset covers the time period from 1981 to 2020 with a 0.25° × 0.25° spatial resolution. More information about the OISST v2.0 data can be found on the website at https://psl.noaa.gov/data/gridded/data.noaa.oisst.v2.highres.html.

The Woods Hole Oceanographic Institution provides the objectively analyzed air–sea fluxes (OAFlux) product (Yu and Weller 2007) for years 1985–2018, including latent and sensible heat fluxes. The SHF is obtained by latent plus sensible heat flux with positive values denoting upward flux from ocean to atmosphere. This product is on a 1° × 1° grid. It was interpolated to 0.25° × 0.25° grids to match the OISST data set. The interpolation from low resolution to high resolution is to retain more signals on small spatial scales, which does not induce the loss of information of SHF distribution as SHF tends to have smoother spatial features. The analysis time period covers from January 1, 1985 to December 31, 2018.

The results obtained from the above SST and SHF data sets are compared with those using Japanese Ocean Flux data sets with Use of Remote Sensing Observations (J-OFURO), obtained from http://dtsv.scc.u-tokai.ac.jp/j-ofuro/, including SST and SHF with a 0.25° × 0.25° spatial resolution. The J-OFURO data set extends from January 1, 1988 to December 31, 2013, which is shorter than OISST and OAFlux datasets. The results are comparable with each other except that the absolute value of correlation coefficients is generally larger based on J-OFURO than based on OISST and OAFlux. This study focus on the results with OISST and OAFlux.

The space smoothing is employed to examine the spatial scale dependence of SHF–SST correlation in this study. A rectangle window running mean from 0.5° to 10° based on the original 0.25° original data is performed in the analysis. If the land grid is included in the calculation of area mean, the grid correlation value remains unchanged. The SST tendency is derived as the central-difference of the daily SST time series. In Sect. 4, the two tailed Student's t test is employed to obtain the level of statistical significance of the correlation between SHF and SST or the SST tendency based on the effective degree of freedom. The critical correlation values are small because of the huge number of the samples using the daily data. The critical correlation coefficient at the 95% confidence level ranges from 0.019 to 0.025 for the SHF–SST correlation and from 0.027 to 0.032 for the SHF–SST tendency correlation. In Sect. 5, the error margins of correlation coefficients are estimated based on the errors of SHF and SST included in the datasets. When calculating the SHF–SST/SST tendency lead–lag correlation at a specific grid, the SST and SHF errors are added to or subtracted from original SST and SHF. As such, four extra correlation coefficients between SST and SHF are obtained. The maximum and minimum values of those correlation coefficient are used to denote the upper and lower limits (error margins) of the corresponding correlation coefficients.

Local grid-point correlation coefficients are calculated for all the months as well as for the winter and summer months. The division of seasons has some difference in Sects. 5 and

6. In Sect. 5, northern winter extends from December 15 to February 14 and northern summer is from June 15 to August 15 to avoid the influence of the other seasons when calculating the lead–lag seasonal correlation between SHF and SST/SST tendency. In Sect. 6, northern winter or southern summer is represented by 5 months extending from November to March in the following year (NDJFM in brief) and northern summer or southern winter covers 5 months from May to September (MJJAS in brief).

Transition length scale L_c has been used to investigate the relative importance of oceanic forcing and atmospheric forcing (Bishop et al. 2017; Small et al. 2019). It was defined as the length scale at which the SHF–SST correlation and SHF–SST tendency correlation is equal when the spatial smoothing is applied. When the length scale L is below L_c, the correlation between SHF and SST is larger than the absolute value of SHF–SST tendency correlation, suggesting a larger SST forcing. On the contrary, the SHF–SST correlation is smaller than the SHF–SST tendency correlation when L is larger than L_c, meaning that the atmospheric forcing dominates the SST change (Bishop et al. 2017).

3 Conceptual model simulations

The conceptual model simulations serve as a basis for understanding the spatial scale dependence of the SHF and SST relationship. Barsugli and Battistis (1998) constructed a stochastic model to measure the effect of air–sea coupling without considering the noise from ocean. Bishop et al. (2017) modified the conceptual stochastic model to include both atmospheric and oceanic noises, which is adopted in this study:

$$\frac{dT_a}{dt} = \alpha\left(T_o - T_a\right) - \gamma_a T_a + N_a, \tag{1}$$

$$\frac{dT_o}{dt} = \beta\left(T_a - T_o\right) - \gamma_o T_o + N_o. \tag{2}$$

In the above equations, subscripts "a" and "o" represents atmosphere and ocean, respectively. T is the surface temperature; α and β are the coefficients of heat flux on the air–sea surface; γ denotes the coefficient of radiative damping; N is the noise from ocean or atmosphere, which is the product of a forcing frequency and a random number that obeys normal distribution and ranges from -1 to 1 ℃. The value of atmospheric forcing frequency ω_a is set to 1×10^{-5} s^{-1}, while the ocean forcing frequency ω_o extends from 1×10^{-7} s^{-1} to 1×10^{-6} s^{-1}. The values of the other parameters are as follows: $\alpha = 23.9 \times 10^{-7}$ s^{-1}, $\beta = 1.195 \times 10^{-7}$ s^{-1}, $\gamma_a = 2.0 \times 10^{-6}$ s^{-1}, and $\gamma_o = 9.5 \times 10^{-9}$ s^{-1} (Barsugli and Battistis 1998; Bishop et al. 2017).

The change of the ocean forcing frequency is used to mimic the change in the ocean advection associated with the SST gradient that varies with the spatial smoothing applied in the observational analysis. In the regions where there are ocean jets such as the WBCs and ARC, ocean advection is a decisive factor to the SST change. According to the mixed layer temperature equation, large advection of SST (representing the vertically averaged temperature) leads to the SST change. This is equivalent to the large oceanic forcing frequency in the simple stochastic model in which the oceanic effect is essential to the SST change. The spatial smoothing reduces the SST gradients and weakens the effect of ocean advection in the SST change, which can be represented as the reduction in the oceanic forcing frequency. In small SST gradient regions, the contribution of oceanic process to the SST change is relatively small. In such regions, strong atmospheric winds may lead to large SHF that has a leading contribution to the SST change and the SHF–SST tendency correlation is expected to be large and thus the atmospheric forcing is likely dominant.

The model results of lead–lag 90-day correlation between SHF and SST and between SHF and the SST tendency are shown in Fig. 1. At large oceanic forcing frequency, the SHF–SST correlation is large positive with the maximum correlation at the SST leading (Fig. 1a), while the SHF–SST tendency correlation is small and displays an asymmetric feature with positive correlation in the leading days and negative correlation in the lagging days (Fig. 1b). With the decrease of the oceanic forcing frequency, the positive SHF–SST correlation decreases and asymmetric features becomes obvious in the SHF–SST correlation with positive correlation at SST leading days and negative correlation at SST lagging days (Fig. 1a). In the meantime, the negative SHF–SST tendency correlation at the zero lag increases as oceanic forcing frequency decreases (Fig. 1b). The above feature indicates that the change in the SHF–SST and SHF–SST tendency correlation signifies the relative importance of oceanic and atmospheric forcing. The oceanic forcing dominates when the positive SHF–SST correlation is large and the SHF–SST tendency correlation is small and asymmetric. The atmospheric forcing becomes important when the SHF–SST correlation weakens and turns to be asymmetric and the negative SHF–SST tendency correlation is large.

4 Comparison of regional correlation between 1° and 4° spatial scale

To illustrate the effect of spatial smoothing on local correlation, Figs. 2 and 3 provide a comparison of SHF–SST/SST tendency correlations in the North Atlantic, North Pacific, Southern Ocean, and tropical North Indian Ocean-western

Fig. 1 The ocean forcing frequency ω_o dependence of lead–lag correlation of SHF–SST (**a**) and SHF–SST tendency (**b**) based on the stochastic model simulations with $\omega_a = 1 \times 10^{-5}$ s^{-1}. X axis represents SST/SST tendency leading (left) and lagging time in days. Y axis represents the ocean forcing frequency ω_o ($\times 10^{-7}$ s^{-1}), ranging from 1×10^{-6} s^{-1} to 1×10^{-7} s^{-1}
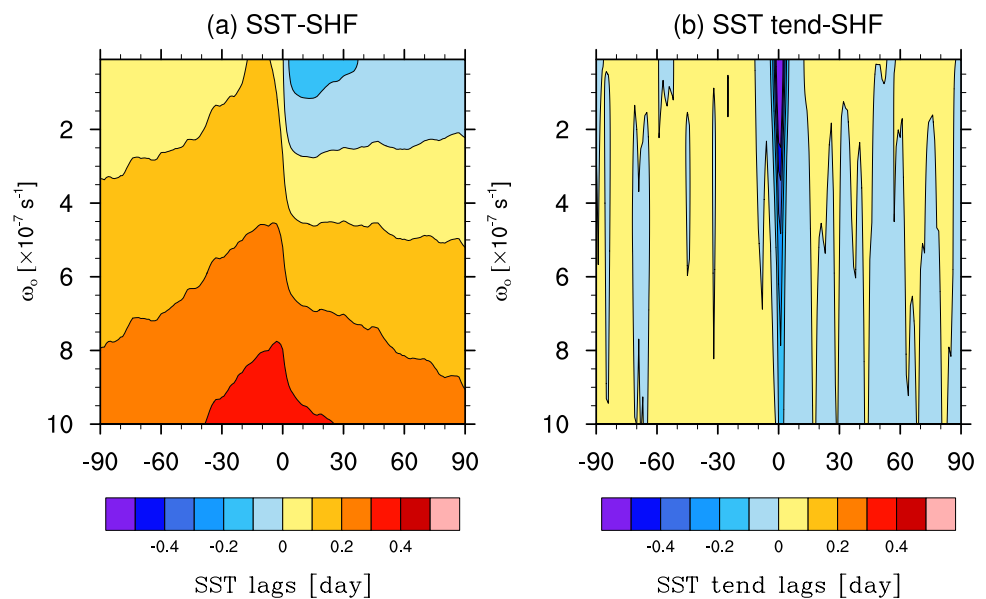
North Pacific between 1° and 4° spatial scale. For 1° spatial scale, the distribution of correlation is similar to Bishop et al. (2017) with monthly data except that the magnitude of the correlation coefficient is not high for most of the regions (< 0.5) because the number of daily samples is huge (12,418 days for 34 years). Large positive SHF–SST correlation between is seen in the Gulf Stream (Fig. 2a), the Kuroshio Extension (Fig. 2c), the ARC (Fig. 2e), and most of the tropical North Indian Ocean-western North Pacific (Fig. 2g). It indicates a remarkable influence of SST on the SHF change (Bishop et al. 2017; Small et al. 2019). When the spatial scale is smoothed to 4° (Fig. 2b, d and f), the positive SHF–SST correlation is much smaller in the WBCs and ARC regions due to the decrease of the SST gradients, meaning that the oceanic effect is weakened. The tropical regions display decrease of correlation from 1° to 4° spatial scale as well (Fig. 2g, h). Compared to the mid-latitude regions, the correlation decrease is not as large in the tropics, which may be attributed to relatively small SST gradient in the tropics so that the spatial smoothing does not lead to a large change in the SST gradient. In the subtropical gyres, the SHF–SST correlation is small negative for 1° and 4° spatial scales. The decrease of the SHF–SST correlation after the spatial smoothing in the WBCs and ARC can also be seen in the correlation calculated for winter (NDJFM/MJJAS) and summer (MJJAS/NDJFM) (not shown).

Interestingly, large SHF–SST correlation appears off the east coast of the Somalia Peninsula for both 1° and 4° spatial scales (Fig. 2g, h). A possible explanation for this is that the northward coastal currents in July and August transport cold water northward (Schott and McCreary 2001), significantly increasing local SST gradient in that region. Furthermore, the SHF–SST correlation off the Somalia Peninsula is larger

in summer than in winter (not shown), which is consistent with the larger SST gradient in summer than in winter over southwestern Arabian Sea (Schott and McCreary 2001). The enhanced SST gradient in summer is associated with the Somali Jet during the South Asian summer monsoon season. The seasonal change in the SHF–SST correlation supports the above explanation.

All the above regions display a negative SHF–SST tendency correlation, and the negative correlation is generally larger in the subtropical gyres than in the WBCs and ARC (Fig. 3). It suggests that away from the WBCs and ARC the atmosphere has a lager influence on the SST change than the regions with rapid ocean currents (Bishop et al. 2017; Small et al. 2019). Compared to the 1° spatial scale, the negative correlation is larger at the 4° spatial scale in most of the regions especially in the subtropical gyres, the South China Sea and the Philippine Sea. This is because the spatial smoothing reduces the SST gradients and weakens the contribution of ocean currents to the SST change and thus the atmospheric influence increases. The effect of the spatial smoothing on local correlation is also seen in the correlation calculated for winter (NDJFM/MJJAS) and summer (MJJAS/NDJFM) (not shown).

5 Spatial scale dependence of lead–lag correlation in winter and summer

The comparison of regional correlation in the mid-latitude ocean and the tropics between 1° and 4° spatial scale in the previous section demonstrates the effect of the spatial smoothing on the air–sea relationship. According to the conceptual model simulations, the relative importance of
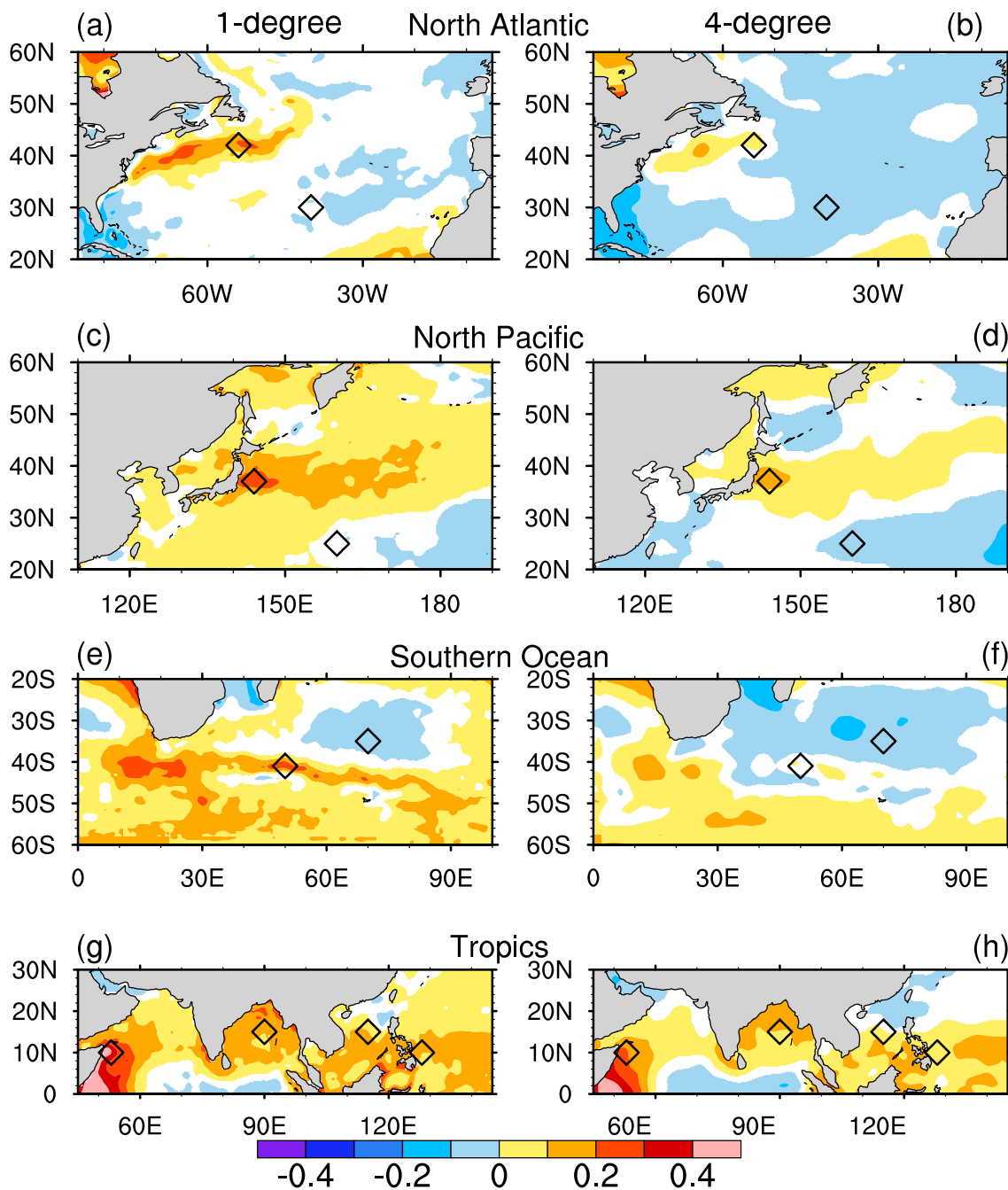
Fig. 2 Simultaneous correlation between SHF and SST calculated based on all the months in the **a, b** North Atlantic, **c, d** North Pacific, **e, f** Southern Ocean and **g, h** tropical North Indian Ocean-western North Pacific for **a, c, e, g** 1° and **b, d, f, h** 4° spatial scale. The two black diamonds in **a–d** are the locations within and outside of the western boundary current extensions. The two black diamonds in **e, f** are the locations within and outside of the Agulhas Return Flow.

The four black diamonds in **g, h** are the locations within the Arabian Sea, the Bay of Bengal, the South China Sea, and the Philippine Sea. The white regions denote correlation coefficient below the 95% confidence level according to the Student t test. The percentage of grid points with correlation coefficient reaching the 95% confidence is about 42% in **a**, 75% in **b**, 82% in **c**, 61% in **d**, 82% in **e**, 73% in **f**, 90% in **g** and 79% in **h**

the oceanic and atmospheric forcing is indicated in the change in the SHF–SST and SHF–SST tendency correlation. The relative strength of the oceanic and atmospheric forcing is associated with the SST gradient. In the

mid-latitude SST frontal zones, the SST gradient varies with the season. Thus, the relative importance of the oceanic and atmospheric forcing differs between winter and summer. The spatial smoothing reduces the SST gradient
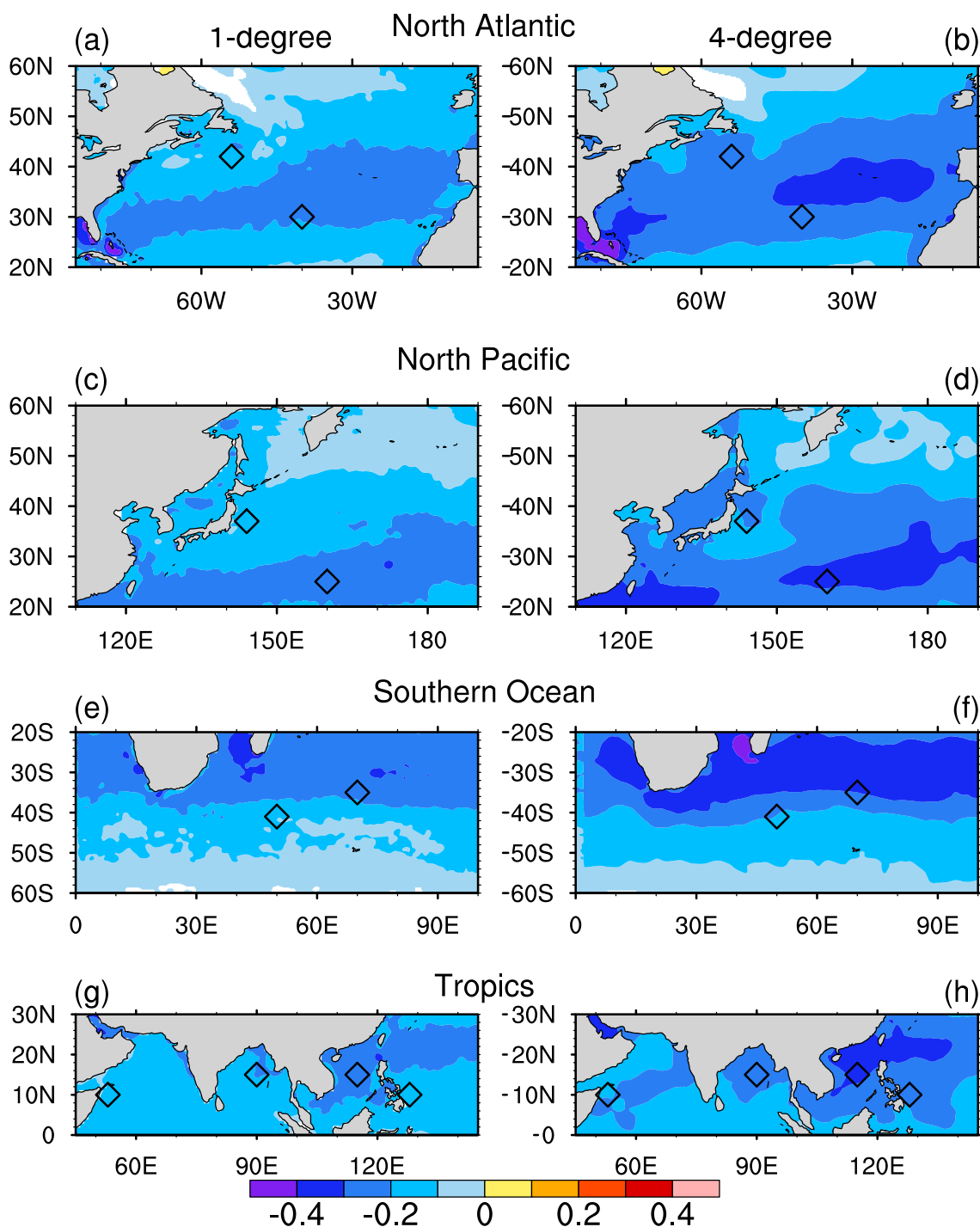
Fig. 3 As Fig. 2 except for the correlation between SHF and SST tendency

and the oceanic process induced SST change and thus the percent contribution of SHF induced SST change increases, leading to a decrease in the oceanic forcing but an increase in the atmospheric forcing as the spatial scale increases. Another effect of spatial smoothing is the removal of small scale unrelated variations, which reduces the standard deviations and leads to an increase

in the SHF–SST tendency correlation as the spatial scale increases.

In this section, we select three locations in the midlatitude SST frontal zones (the Gulf Stream, the Kuroshio Extension, and the ARC), three locations in the midlatitude subtropical gyres (the North Atlantic, the North Pacific, and the Southern Ocean), and four points in the tropical North

Indian Ocean-western North Pacific (the Arabian Sea, the Bay of Bengal, the South China Sea, and the Philippine Sea), which are denoted by the black diamonds in Fig. 2. The selection of the grid points in the mid-latitude SST frontal zones and subtropical gyres follows previous studies (Bishop et al. 2017; Sun and Wu 2021). According to Bishop et al. (2017), Small et al. (2019), and Sun and Wu (2021), those grid points can represent distinct oceanic and atmospheric forcing cases in the three ocean basins. The grid points in the Bay of Bengal and the South China Sea are the same as those in Sun and Wu (2021). The grid point in the Arabian Sea is closer to the large SST gradient region than that in Sun and Wu (2021). The grid point in the Philippine Sea is closer to the Inter-tropical Convergence Zone compared to that in Sun and Wu (2021). The seasonal lead–lag SHF–SST and SHF–SST tendency correlations at different spatial smoothing were presented for the WBCs and ARC (Figs. 4 and 5), the Subtropical Gyres (Figs. 9 and 10), and the tropical North Indian Ocean-western North Pacific (Figs. 11 and

12) to inspect the spatial scale dependence of lead–lag correlation in different seasons. The lead–lag SHF–SST/SST tendency correlation curves at the WBCs and ARC in winter and summer for 1°, 4°, and 8° spatial scales are shown (Figs. 6, 7 and 8) to inspect the seasonal difference of the spatial scale dependence of the air–sea relationship. The lead–lag SHF–SST/SST tendency correlations in the Arabian Sea and the Philippine Sea in summer are compared (Fig. 13) to examine the regional difference of the spatial scale dependence of air–sea interaction in the tropics.

In the mid-latitude regions during winter, the positive SHF–SST correlation is as large as 0.3–0.4 and shows a symmetric pattern about 2–4 SST leading days below 3° spatial scale (Fig. 4a–c). The SHF–SST tendency correlation is small with asymmetric feature at small spatial scales (Fig. 4d–f). These features resemble the conceptual model simulation when the ocean forcing frequency is large (Fig. 1). This indicates a dominant oceanic forcing. Above 3° spatial scale, the positive SHF–SST correlation becomes
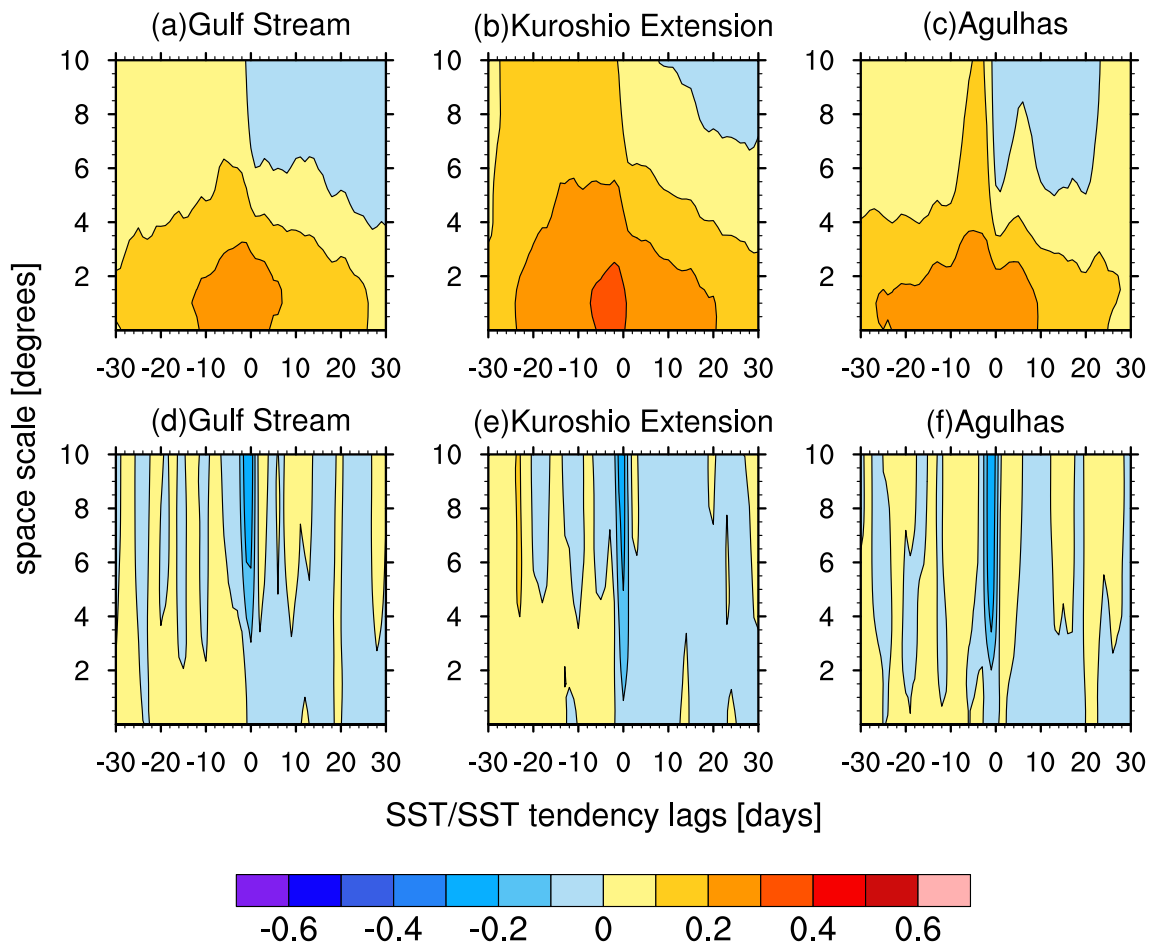

Fig. 4 Space-scale dependence of lead–lag **a–c** SHF–SST and **d–f** SHF–SST tendency correlation using daily and 0.25°–10° rectangle moving mean data at the black diamond locations **a**, **d** within the Gulf Stream, **b**, **e** within the Kuroshio Extension, and **c**, **f** within the Agulhas Return Flow in Fig. 2 in winter (DJF in **a**, **b** and **d–f**, JJA in **c** and **f**. X axis represents SST/SST tendency leads (left) and lags (right) in days. Y axis represents the spatial scale in degrees
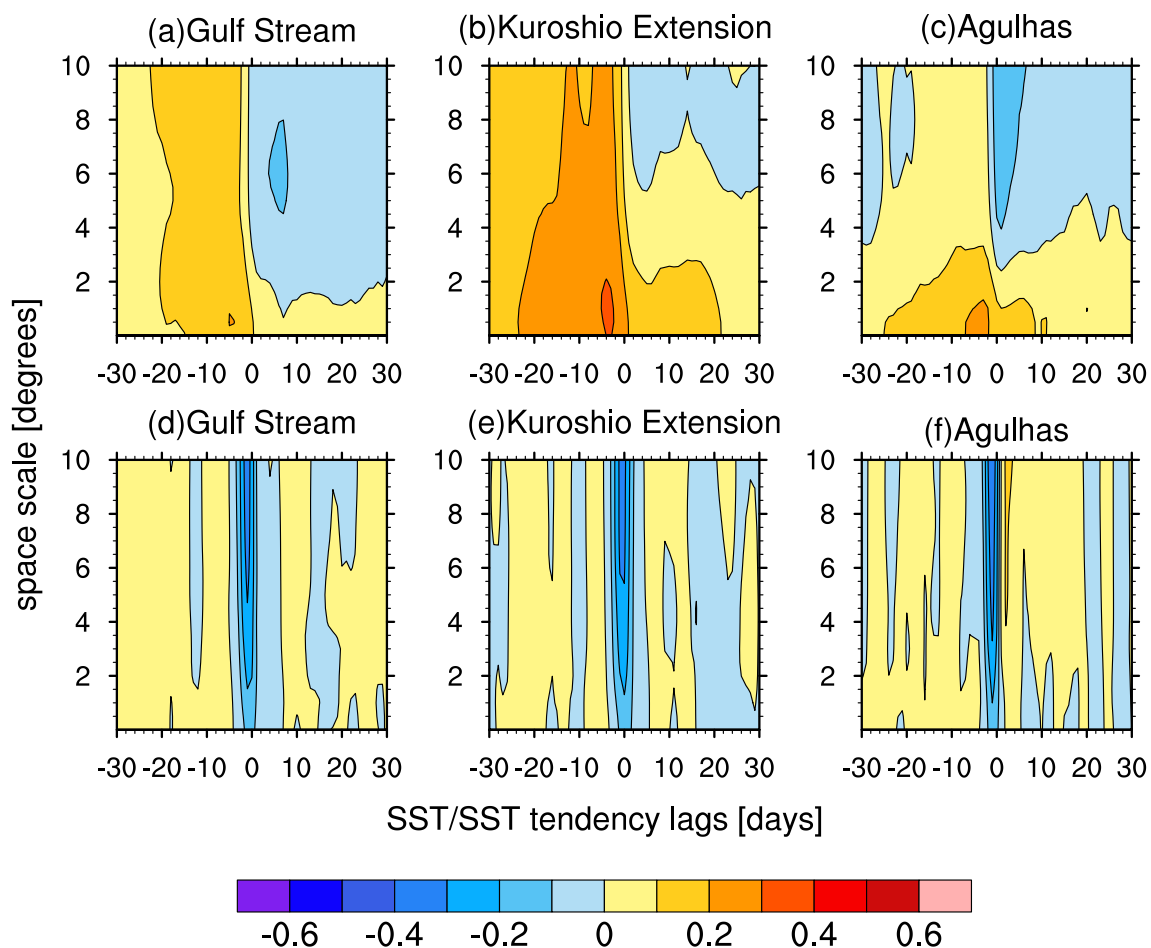
Fig. 5 As Fig. 4 except in summer (JJA in **a**, **b** and **d**, **e**, DJF in **c** and **f**)

small and the lead–lag correlation structure switches from symmetric to asymmetric when the spatial scale reaches above 6°. In the meantime, the simultaneous negative SHF–SST tendency increases largely. The features become similar to the conceptual model results with small ocean forcing frequency (Fig. 1). This signifies the atmospheric driving of the SST change. The above analysis suggests a switch from the oceanic forcing to the atmospheric forcing around the 3°–5° spatial scale in the WBCs and ARC in winter. Phenomenologically, it tells the spatial scale at which the strength of oceanic and atmospheric forcing becomes comparable. This special spatial scale is determined by the magnitude and change with the spatial scale of SHF–SST and SHF–SST tendency correlations, which will be discussed later in Sect. 6.

In the mid-latitude regions during summer, the maximum positive SHF–SST correlation is seen at 1°–2° spatial scale at SST leading around 5 days (Fig. 5a–c). The magnitude of positive SHF–SST correlation is smaller compared to that in winter. The correlation becomes smaller as the spatial scale increases. The asymmetric

pattern shows up at 2° scale at the Gulf Stream (Fig. 5a), 6° scale at the Kuroshio Extension (Fig. 5b), and 3° scale at the Agulhas Return Flow (Fig. 5c). For the lead–lag correlation between SHF and the SST tendency (Fig. 5d–f), the structure is similar to that in winter. In comparison, the simultaneous negative SHF–SST tendency correlation is larger in summer than in winter. The above differences in the magnitude, scale and lead time of the maximum SHF–SST correlation and in the magnitude of the maximum SHF–SST tendency correlation are all indicative of a weakening of the oceanic forcing from winter to summer, which is similar to the conceptual model results (Fig. 1). This change is related to the decrease of the SST gradients in the mid-latitude frontal zones from winter to summer (Table 1), which weakens the contribution of ocean advection to the SST change and enhances the relative contribution of SHF to the SST change. This means that the atmosphere has a larger impact on the SST change in summer for the three locations. The difference in the spatial scale when the asymmetric pattern becomes obvious may be associated with the regional change in the magnitude
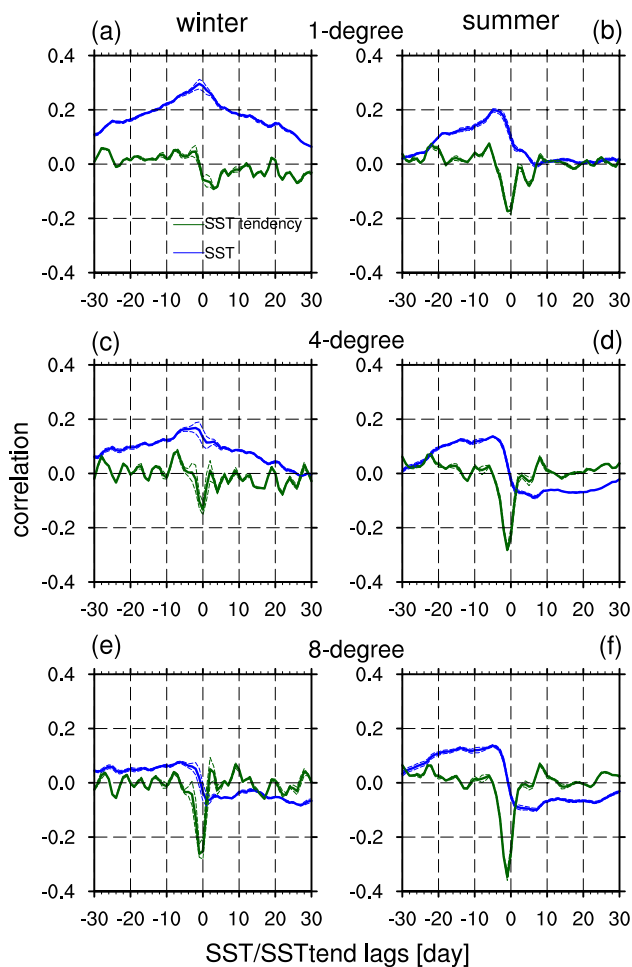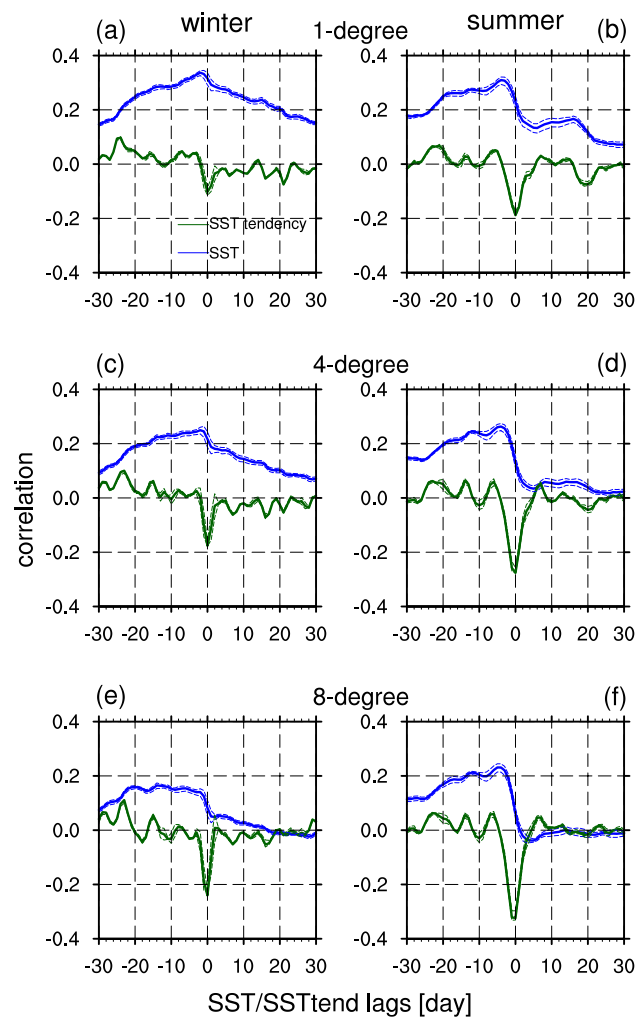
Fig. 6 Lead–lag correlation of SHF–SST (blue curves) and SHF–SST tendency (green curves) at the black diamond locations within the Gulf Stream in Fig. 2 in **a**, **c**, **e** winter (DJF) and **b**, **d**, **f** summer (JJA) for **a**, **b** 1°, **c**, **d** 4° and **e**, **f** 8° spatial scale. Dashed lines denote the error margins of correlation coefficients. X axis represents SST/SST tendency leading (left) and lagging (right) time in days. Y axis represents the correlation coefficient

Fig. 7 Lead–lag correlation of SHF–SST (blue curves) and SHF–SST tendency (green curves) at the black diamond locations within the Kuroshio Extension in Fig. 2 in **a**, **c**, **e** winter (DJF) and **b**, **d**, **f** summer (JJA) for **a**, **b** 1°, **c**, **d** 4° and **e**, **f** 8° spatial scale. Dashed lines denote the error margins of correlation coefficients. X axis represents SST/SST tendency leading (left) and lagging (right) time in days. Y axis represents the correlation coefficient

of the SST gradients that affects the spatial scale when the atmospheric forcing becomes dominant. This will be discussed in Sect. 6.

To further illustrate the effect of the spatial scale and the seasonal difference, we show in Figs. 6, 7 and 8 the SHF–SST/SST tendency correlation at the WBCs and ARC at three spatial scales in winter and summer, which is extracted from Figs. 4 and 5. At the Gulf Stream in winter, the SHF–SST correlation reaches a peak as high as 0.3 at 1-day SST leading for 1° spatial scale and the lead–lag correlation is symmetric (Fig. 6a). The SHF–SST tendency correlation is smaller than the SHF–SST correlation, displaying a positive-negative asymmetric pattern about zero lag with fluctuations with the lead–lag time due to the high frequency feature of the daily data. For 4° spatial scale, the peak SHF–SST correlation decreases to below 0.2 at 2-day

SST leading and the largest negative SHF–SST tendency increases to above 0.1 and appears at the zero lag (Fig. 6c). When the spatial scale reaches 8°, the lead–lag correlation between SHF and SST/SST tendency presents the atmosphere-driven feature with small and asymmetric SHF–SST correlation and large simultaneous negative SHF–SST tendency correlation (Fig. 6e). Similar changes with the spatial scale in the SHF–SST/SST tendency correlations are observed at the Kuroshio Extension and the Agulhas Return Flow in winter (Figs. 7a, c, e, and 8a, c, and e). The changes of lead–lag correlation curves for the three spatial scales signify that the transition of air–sea relationship from ocean-driven to atmosphere-driven when the spatial scale increases in winter. Such changes are associated with the
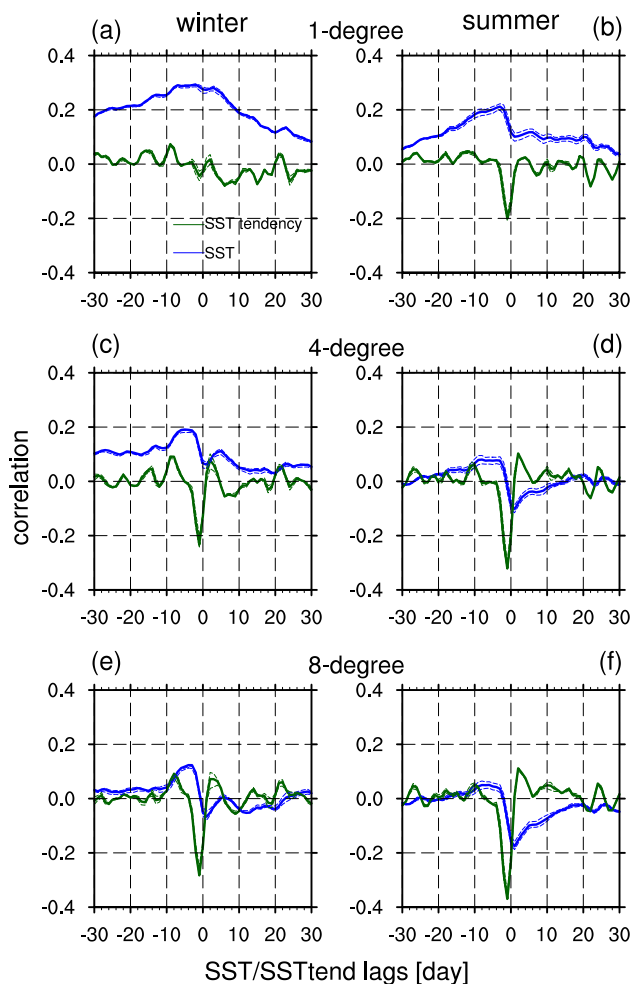
Fig. 8 Lead–lag correlation of SHF–SST (blue curves) and SHF–SST tendency (green curves) at the black diamond locations within the Agulhas Return Flow in Fig. 2 in **a**, **c**, **e** winter (JJA) and **b**, **d**, **f** summer (DJF) for **a**, **b** 1°, **c**, **d** 4° and **e**, **f** 8° spatial scale. Dashed lines denote the error margins of correlation coefficients. X axis represents SST/SST tendency leading (left) and lagging (right) time in days. Y axis represents the correlation coefficient

decrease of the SST gradients when spatial smoothing is applied (Table 1), which reduces the contribution of oceanic processes to the SST change, but enhances the relative role of SHF in the SST change.

At the Gulf Stream in summer, the SHF–SST correlation reaches the highest at 4-day lead and the SHF–SST tendency correlation reaches the lowest at zero lead for 1° spatial scale (Fig. 6b), which indicates the contribution of both oceanic and atmospheric processes to the SST change. For 4° spatial scale, the simultaneous negative SHF–SST tendency correlation is large and the SHF–SST correlation is asymmetric (Fig. 6d), indicative of the atmosphere-driven dominance, which is similar to Fig. 6e. As the spatial scale increases to 8°, the atmosphere-driven feature remains and the simultaneous negative SHF–SST tendency correlation increases to

over −0.3 (Fig. 6f). Similar changes with the spatial scale in the SHF–SST/SST tendency correlations are seen at the Kuroshio Extension and the Agulhas Return Flow in summer with some differences in the magnitude of the correlations (Figs. 7b, d and f and 8b, d and f). As in winter, the lead–lag correlation changes for the three spatial scales in summer reveal the spatial scale dependence of the air–sea relationship. Differences from winter are noted in the spatial scale of transition to the atmospheric forcing: smaller in summer and larger in winter. The difference is related to the seasonal change in the magnitude of the SST gradient (Table 1). The smaller SST gradient in summer tends to be followed by a switch at smaller spatial scales from the oceanic forcing to the atmospheric forcing in summer than in winter.

In the Subtropical Gyre regions, the lead–lag SHF–SST correlation displays positive-negative asymmetric pattern about zero lag, and the magnitude of positive and negative correlation changes only slightly with the spatial smoothing in both winter and summer (Figs. 9a–c and 10a–c). For the lead–lag SHF–SST tendency correlation, large negative correlation shows between ±2 lead days and is enhanced with the spatial scale increase in both winter and summer (Figs. 9d–f and 10d–f). This implies that the atmosphere forcing dominates in the subtropical gyre regions for all the spatial scales and the forcing intensifies with the spatial scale increase. In comparison, the negative SHF–SST tendency correlation is larger in summer than in winter, indicative of a larger atmospheric forcing in summer compared to winter. This difference is related to a shallower mixed-layer depth in the subtropical regions in summer than in winter (Wu et al. 2015).

In the tropical North Indian Ocean and western North Pacific, in winter, the lead–lag SHF–SST correlation displays a positive-negative asymmetric pattern about zero lag with slight change with the spatial scale (Fig. 11a–d). The simultaneous SHF–SST tendency correlation is large negative with the magnitude increasing with the spatial scale (Fig. 11e–h). The above features indicate that the atmospheric forcing is important from 0.25° to 10° spatial scale in the above regions. This is due to small SST gradients in the tropical region so that the contribution of oceanic processes to the SST change is relatively small and SHF has a dominant role in the SST change. The spatial scale dependence of correlation between SHF and SST or SST tendency in the above tropical regions is not as obvious as in the WBCs and ARC since the spatial smoothing does not lead to a notable change in the SST gradient-related oceanic forcing in the tropics.

In the Bay of Bengal, South China Sea, and Philippine Sea, in summer, the SHF–SST correlation is asymmetric (Fig. 12b–d) and the simultaneous SHF–SST tendency correlations is negative (Fig. 12f–h), indicative of atmospheric forcing. This feature is related to the small SST gradient
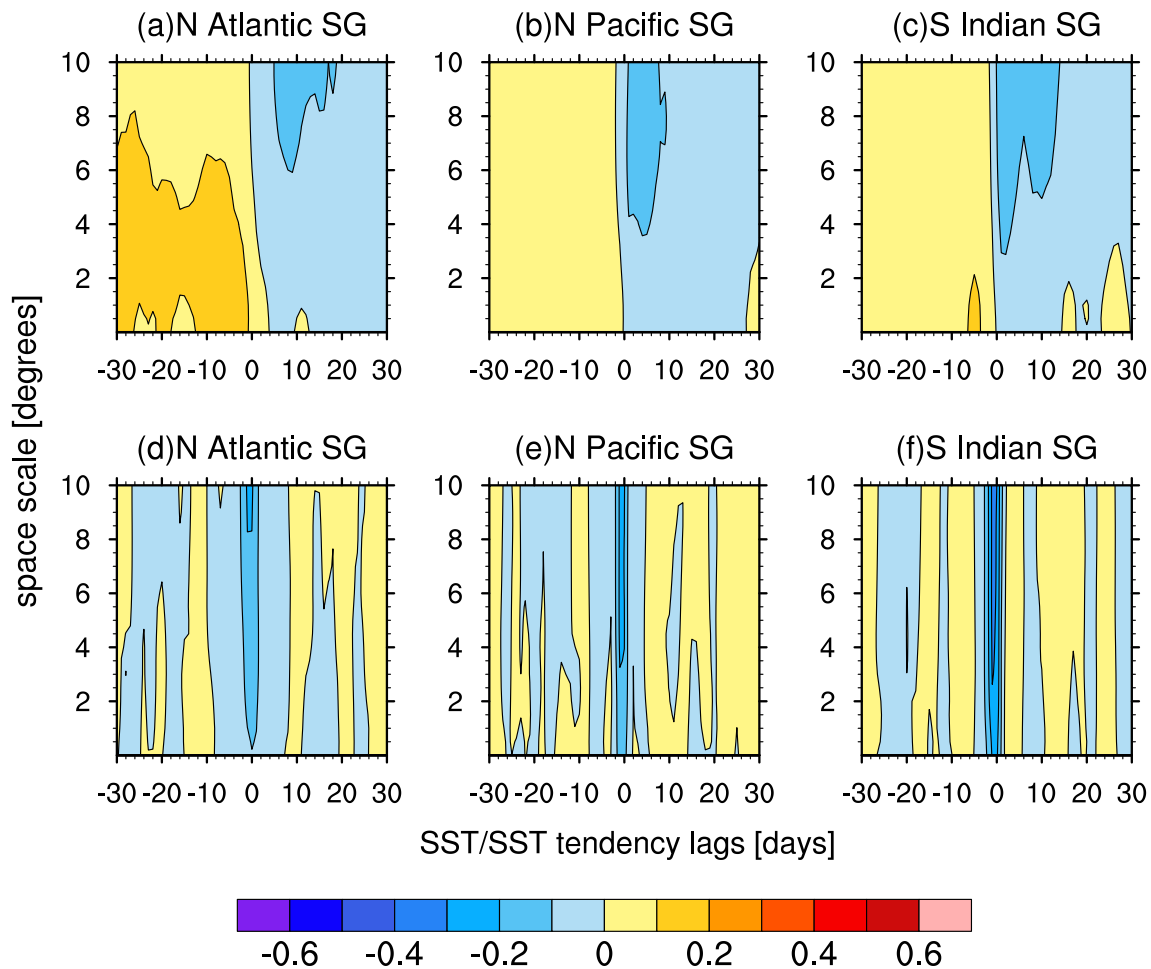
Fig. 9 Space-scale dependence of lead–lag **a–c** SHF–SST and **d–f** SHF–SST tendency correlation using daily and 0.25°–10° rectangle moving mean data at the black diamond locations **a**, **d** within the North Atlantic subtropical gyre, **b**, **e** within the North Pacific sub- tropical gyre, and **c**, **f** within the southern Indian Ocean subtropical gyre in Fig. 2 in winter (DJF in **a**, **b** and **d–f**, JJA in **c** and **f**. X axis represents SST/SST tendency leads (left) and lags (right) in days. Y axis represents the spatial scale in degrees

in those regions. The magnitude of the SHF–SST correlation changes little with the spatial scale in the three regions (Fig. 12b–d) as the spatial smoothing does not lead to notable change in the oceanic forcing in small SST gradient regions. The magnitude of the SHF–SST tendency correlation displays an increase with the spatial scale in the South China Sea and Philippine Sea (Fig. 12g–h), which may be due to the effect of spatial smoothing that removes small scale unrelated variations and reduces the standard deviations. For example, at the grid point of the South China Sea, the standard deviation of the SST tendency in winter (summer) is 0.39 (0.45) and 0.23 (0.23) °C/month, respectively, at 1° and 8° spatial scale. In the Arabian Sea, the SHF–SST correlation is large positive and symmetric (Fig. 12a) and the SHF–SST tendency correlation is asymmetric in summer (Fig. 12e). This is a typical oceanic forcing pattern, which may be attributed to the large SST gradient in this region during the South Asian summer monsoon season.

The positive SHF–SST correlation reaches the largest below 2° spatial scale and is decreases as the spatial scale increases (Fig. 12a). The asymmetric SHF–SST tendency correlation is maintained as the spatial scale increases (Fig. 12e).

The above analysis shows a distinctive feature of the air–sea relationship in summer in the Arabian Sea from the other tropical regions. To further illustrate this, we compare in Fig. 13 the correlation in summer for three spatial scales in the Arabian Sea and the Philippine Sea. In the Arabian Sea, the SHF–SST correlation displays symmetric pattern about zero lag at all the three spatial scales (Fig. 13a, c and e). The magnitude of the maximum correlation coefficient decreases from 0.8 at 1° to 0.5 at 8° spatial scale. At 8° scale, the lead–lag correlation shows asymmetric feature (Fig. 13e). At 1° scale, the SHF–SST tendency correlation displays asymmetric feature about zero lag with the maximum value about 0.2 and the minimum value about −0.25 (Fig. 13a). At 4° and 8° scales, the SHF–SST tendency correlation is
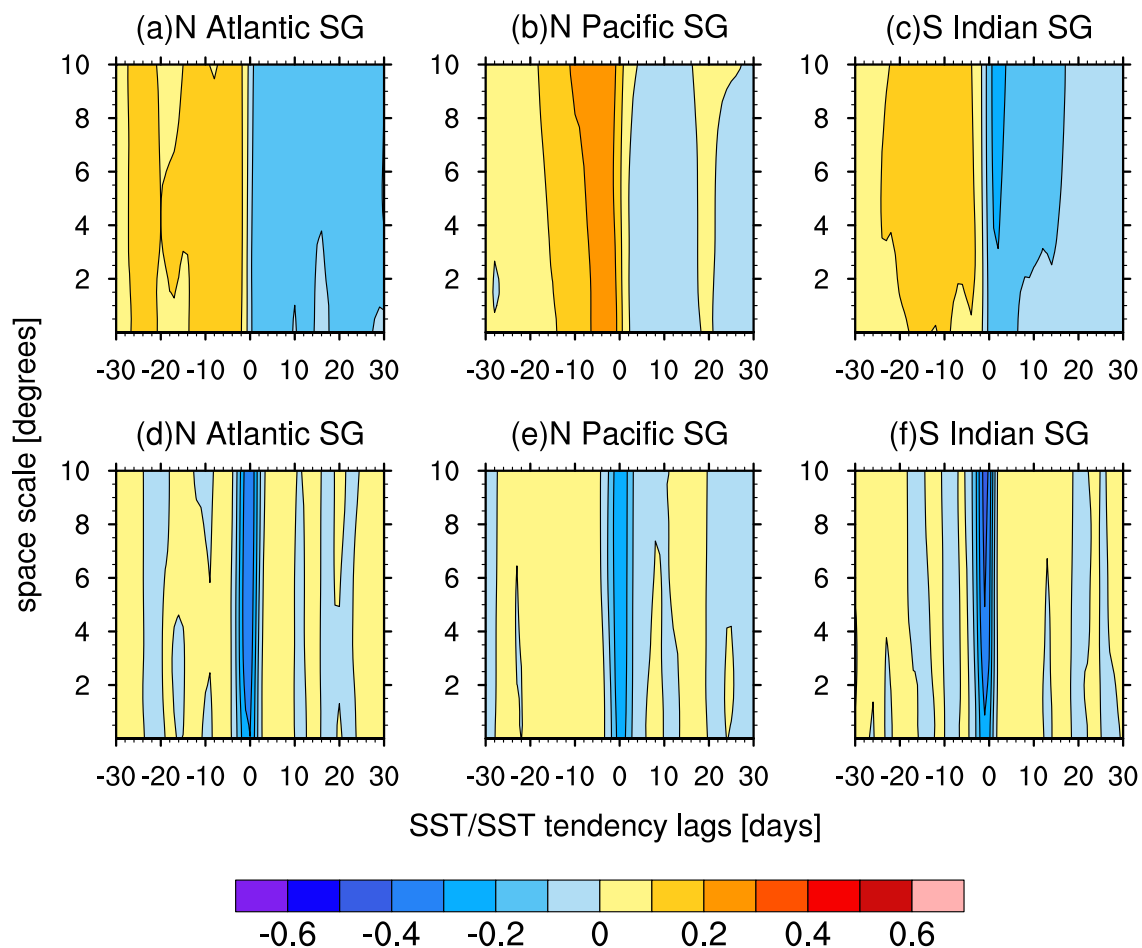
Fig. 10 As Fig. 9 except in summer (JJA in **a**, **b** and **d**, **e**, DJF in **c** and **f**)

also asymmetric, but the maximum correlation values are smaller than 0.2 (Fig. 13c and e). These details illustrate that in the Arabian Sea during summer, the oceanic forcing of the SST change decreases as the spatial scale increases. In the Philippine Sea, the lead–lag correlation curves show atmospheric-forcing pattern with the simultaneous negative SHF–SST tendency correlation increasing from − 0.2 at 1° spatial scale to − 0.3 at 8° spatial scale (Fig. 13b, d and f). This suggests that the influence of atmosphere increases gradually as the spatial scale increases. The above comparison of correlation among the three spatial scales indicates limited changes of the air–sea relationship with the spatial scale in the tropics in summer. However, the ocean has a major influence on the SST change in the Arabian Sea, while the atmosphere-driven pattern dominates in the Philippine Sea. The difference between the Arabian Sea and the Philippine Sea may be explained by the SST gradient. In the Arabian Sea, the northward coastal currents in summer transport cold water northward (Schott and McCreary 2001), leading to large SST gradient so that oceanic advection contributes largely to the SST change. In contrast, the Philippine Sea

is in the western Pacific warm pool region where the SST gradient is small so that the oceanic process plays a minor role in the SST change. On the other hand, high-frequency atmospheric fluctuations are large in the western Pacific warm pool region and thus SHF has a large effect on the SST change (Wu et al. 2015; Wu and Chen 2015; Wu 2016).

6 Transition length scale at different locations and seasons

Section 5 illustrates that in the WBCs and ARC, the lead–lag correlation structure transforms from ocean-driven to atmosphere-driven with spatial smoothing in both winter and summer. To determine the specific spatial scale for the switch from the oceanic forcing to atmospheric forcing, Bishop et al. (2017) compared the magnitude of SHF–SST and SHF–SST tendency correlation coefficients with spatial smoothing and defined the transition length scale L_c with monthly data. Using the same method, we determine the transition length scale using daily data in different seasons at
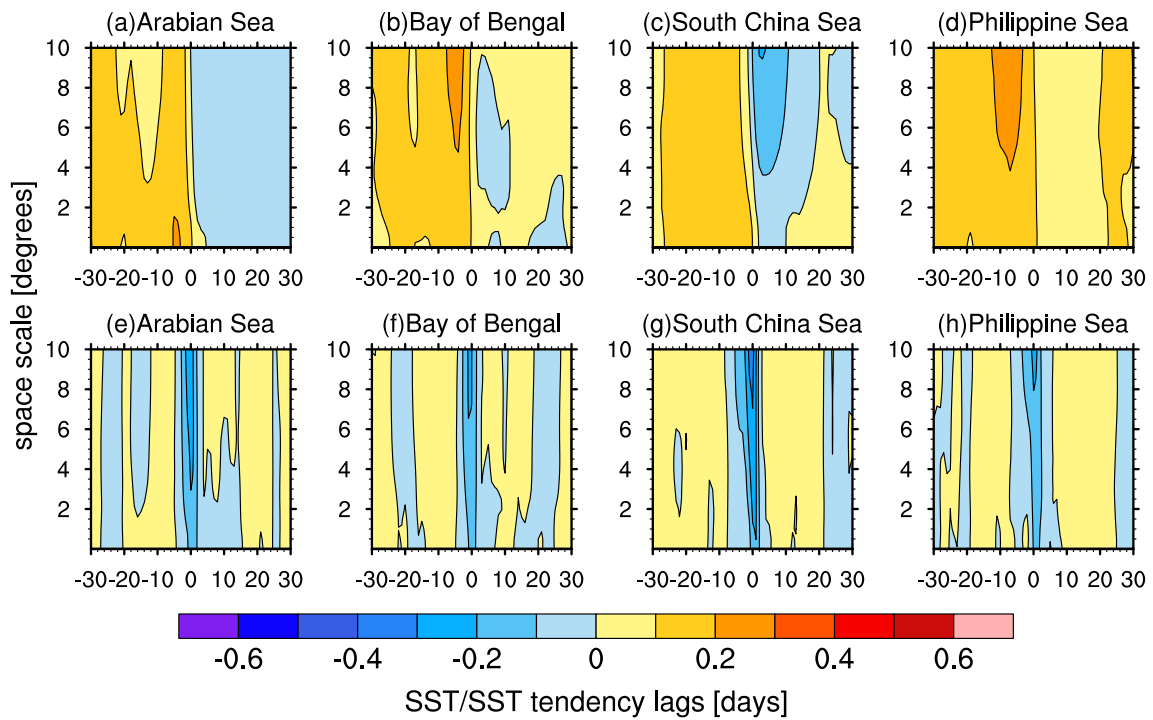
Fig. 11 Space-scale dependence of lead–lag **a–c** SHF–SST and **d–f** SHF–SST tendency correlation using daily and 0.25°–10° rectangle moving mean data at the black diamond locations **a**, **e** within the Arabian Sea, **b**, **f** within the Bay of Bengal, **c**, **g** within the South China Sea, and **d**, **h** within the Philippine Sea in Fig. 2 in winter (DJF). X axis represents SST/SST tendency leads (left) and lags (right) in days. Y axis represents the spatial scale in degrees
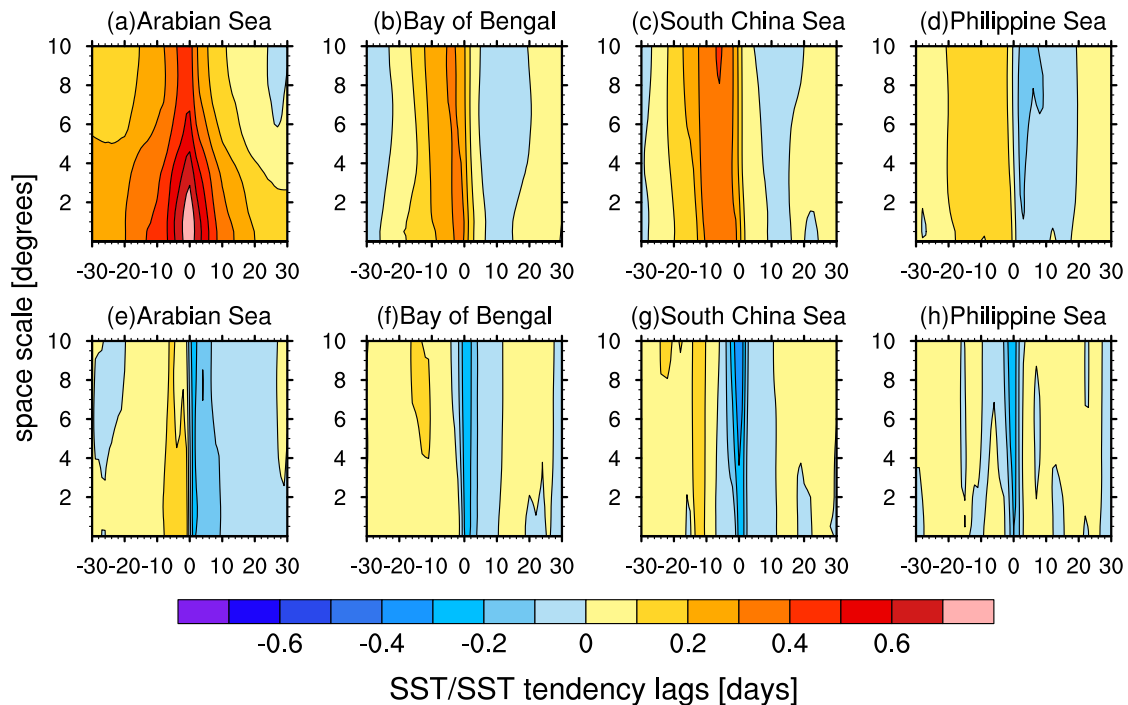

Fig. 12 As Fig. 11 except in summer (JJA)
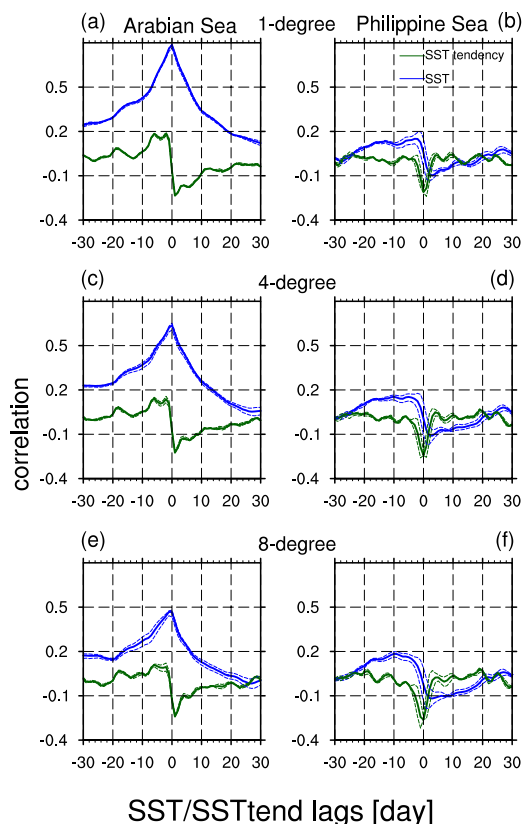
Fig. 13 Lead–lag correlation of SHF–SST (blue curves) and SHF–SST tendency (green curves) at the black diamond locations **a**, **c**, **e** within the Arabian Sea and **b**, **d**, **f** within the Philippine Sea in Fig. 2 in summer (JJA) for **a**, **b** 1°, **c**, **d** 4° and **e**, **f** 8° spatial scale. Dashed lines denote the error margins of correlation coefficients. X axis represents SST/SST tendency leading (left) and lagging (right) time in days. Y axis represents the correlation coefficient

Fig. 14 Method for determining the transition length scale L_c. Thick curves with dots are polynomial fitting lines of simultaneous SHF–SST correlation and thin curves with open circles are polynomial fitting lines of simultaneous SHF–SST tendency correlation (absolute value) using daily data at the WBC locations in **a** winter (NDJFM for the Gulf Stream and the Kuroshio Extension and MJJAS for the Agulhas Return Flow) and **b** summer (MJJAS for the Gulf Stream and the Kuroshio Extension and NDJFM for the Agulhas Return Flow). X axis represents the spatial scale in degrees. Y axis represents the correlation coefficient

the selected points in the Gulf Stream, Kuroshio Extension, ARC, and tropical North Indian Ocean and western North Pacific (the points are the same with Sect. 5). The results are presented in Figs. 14 and 15; Table 1 for winter and summer.

According to the definition of the transition length scale, the value of L_c depends upon the magnitude and pace of change with the spatial scale of SHF–SST and SHF–SST tendency correlations. The magnitude of the two correlation coefficients is associated with the magnitude of the SST gradient that varies with season and location. The pace of decrease/increase of correlations is related to how fast

the magnitude of the SST gradient changes with the spatial smoothing scale. A faster decrease of the SST gradient with the increase of spatial scale is expected to be followed by a smaller transition length scale.

In the WBCs and ARC, the SHF–SST correlation decreases and the absolute SHF–SST tendency correlation increases as the spatial scale increases (Fig. 14). The L_c is generally larger in winter than in summer (Fig. 14; Table 2). In winter, the transition length scale is 2.6° (2.2°–3.2°) in the Gulf Stream, 4.5° (3.9°–5.8°) in the Kuroshio Extension, and

Table 1 Meridional SST gradient (°C/degree latitude) in winter and summer for 1, 4 and 8-° spatial scale. The longitude range for average is 301°–311° E for the Gulf Stream, 143° 153° E for the Kuroshio Extension, and 45° 55° E for the Agulhas Return Flow

Location	Gulf stream			Kuroshio extension			Agulhas return flow		
Spatial scale	1	4	8	1	4	8	1	4	8
Winter	− 1.19	− 0.81	− 0.52	− 0.42	− 0.41	− 0.39	0.64	0.53	0.34
Summer	− 0.77	− 0.56	− 0.38	− 0.28	− 0.26	− 0.26	0.56	0.48	0.35

3.0° (2.8°–3.2°) in the Agulhas Return Flow (Table 2). In summer, the transition length scale is 0.9° (0.3°–1.5°) in the Gulf Stream, 1.0° (0.5°–1.6°) in the Kuroshio Extension, and 1.3° (0.9°–1.8°) in the Agulhas Return Flow (Table 2). The seasonal difference in the transition length scale is because the SHF–SST correlation is larger in winter than in summer (Fig. 14) due to the larger SST gradient in winter than in summer (Table 1). As such, the atmospheric forcing starts to dominate at a smaller spatial scale in summer than in winter. There is also a regional difference in the L_c value. The Gulf Stream has the smallest L_c in both winter (2.6°) and summer (0.9°), while the largest L_c in winter is in the Kuroshio Extension (4.5°) and in summer is the Agulhas return flow (1.3°). Such regional difference is a result of the magnitude and change with the spatial scale of the SST gradient among the three regions. For example, the SST gradient at 1° (8°) spatial scale in winter is − 1.19 °C (− 0.52 °C) per degree latitude in the Gulf Stream and −0.42° (−0.39°) per degree latitude in the Kuroshio Extension. The faster decrease of the SST gradient in the Gulf Stream leads to a faster weakening of the oceanic forcing, accounting for the smaller transition length compared to that in the Kuroshio Extension. The different pace of decrease of the SST gradient with the spatial smoothing is attributed to meridional extension of the SST front, which is narrower in the Gulf Stream than in the Kuroshio Extension.

The tropical North Indian Ocean and western North Pacific locations show no crossing points between the SHF–SST and SHF–SST tendency correlation curves in winter (Fig. 15a). Thus, no L_c exists at the four locations in winter. The possible reasons have been mentioned in Sect. 4. In the tropics, the heat content is well-distributed and the SST gradients are small so that the spatial smooth-

Table 2 Transition length scale and its upper and lower bounds in degree at WBCs and ARC in winter and summer based on OISST and OAFlux data

Location	Gulf stream	Kuroshio extension	Agulhas return current
Winter	2.6 (2.2–3.2)	4.5 (3.9–5.8)	3.0 (2.8–3.2)
Summer	0.9 (0.3–1.5)	1.0 (0.5–1.6)	1.3 (0.9–1.8)

ing has limited influence on the correlation in the tropical regions. In winter, the SHF–SST and SHF–SST tendency correlation curves in the four locations change with the spatial scale relatively smoothly compared to those in the mid-latitude regions and the atmospheric forcing is prominent for all the examined spatial scales (Fig. 15a). In summer, in the Arabian Sea, the SHF–SST correlation is larger than the SHF–SST tendency correlation up to 10° spatial scale (Fig. 15b). In the Bay of Bengal, South China Sea,
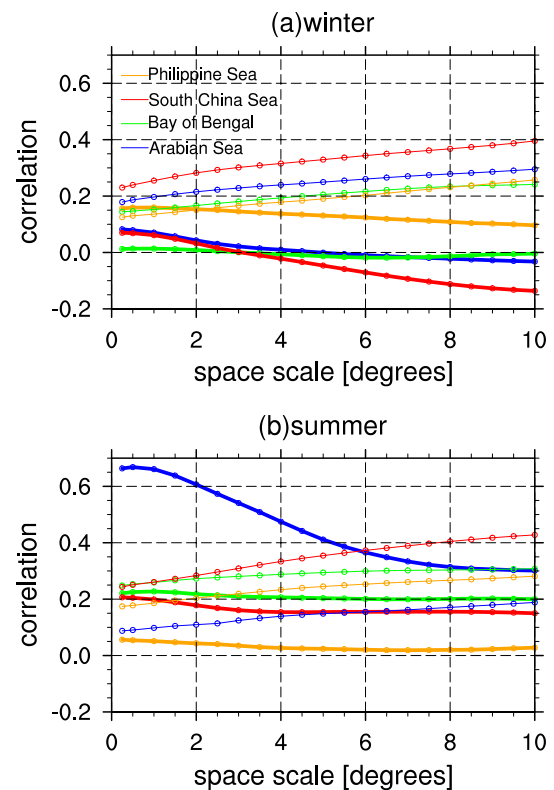

Fig. 15 As Fig. 14 except at the tropical North Indian Ocean and western North Pacific locations in **a** winter (NDJFM) and **b** summer (MJJAS)

and Philippine Sea, the magnitude of SHF–SST tendency correlation is larger than the SHF–SST correlation for all the examined spatial scales with the difference increasing with the spatial scale (Fig. 15b), which is opposite to that in the Arabian Sea.

7 Summary and discussions

This study investigates the spatial scale dependence of the SHF–SST and SHF–SST tendency correlation in different regions in winter and summer with daily data. The spatial scale dependence is illustrated by a comparison of the correlation for 1° and 4° spatial smoothing. For 1° spatial scale, the SHF–SST correlation is positive in the WBCs, ARC, and most of the tropical North Indian Ocean-western North Pacific, suggesting the oceanic forcing at small spatial scales in these regions. With 4° spatial smoothing, the magnitude of SHF–SST correlation decreases and the positive correlation areas are reduced due to the decrease of SST gradients. The SHF–SST tendency correlation is negative in all the above regions and in the subtropical gyres. The negative correlation is larger at 4° spatial scale than at 1° spatial

scale due to the weakened influence of the ocean after spatial smoothing.

The spatial scale dependence of the air–sea relationship displays notable difference between winter and summer in the mid-latitude oceanic fronts. In winter, the SHF–SST correlation is large positive, which is accompanied by small simultaneous negative SHF–SST tendency correlation at the selected points in the Gulf Stream, Kuroshio Extension, and ARC for less than 3° spatial scales. Above 3° spatial scales, the SHF–SST correlation decreases in magnitude and switches to positive–negative asymmetric distribution at around 6° scale. Meanwhile, the simultaneous negative SHF–SST tendency correlation increases with the spatial scale. This means that the oceanic forcing is critical below 3° spatial scale and the atmosphere-driven feature is predominant for large spatial scale in the WBCs and ARC in winter. In summer, the positive SHF–SST correlation is relatively small and the transition from the oceanic forcing to the atmospheric forcing occurs at a smaller spatial scale than in winter.

In the Bay of Bengal, South China Sea, and Philippine Sea, the SHF–SST correlation changes little with the spatial scale with asymmetric feature in both winter and summer. The simultaneous SHF–SST tendency correlation is negative with the magnitude increasing with the spatial scale in both winter and summer. Thus, at these three regions, the atmospheric forcing is significant for all the spatial scales in winter and summer with the magnitude increasing with the spatial scale. In comparison, the atmospheric forcing is larger in summer than in winter in those regions. In the Arabian Sea, the change of the SHF–SST and SHF–SST tendency correlation with the spatial scale is not obvious as well in winter. In summer, the oceanic forcing predominates up to 10° spatial scale with the magnitude weakening slightly with the increase of the spatial scale.

The seasonal and regional differences in the spatial scale dependence of the SHF–SST and SHF–SST tendency correlations in the mid-latitude SST frontal zones may be explained by the changes in the SST gradient. The larger SST gradient in winter than in summer leads to a stronger oceanic forcing in winter than in summer and a larger spatial scale for the switch from the oceanic forcing to the atmospheric forcing. The reduction of the SST gradient with the spatial smoothing accounts for the decrease of oceanic forcing and the increase of atmospheric forcing as the spatial scale increases. The smaller transition length scale in the Gulf Stream than in the Kuroshio Extension is attributed to a faster decrease of the oceanic forcing with the spatial scale in the former region than in the latter region. The small SST gradient in the tropical regions explains the dominance of atmospheric forcing in the tropics except for the Arabian Sea in summer. The increase of the SHF–SST tendency correlation with the spatial scale in the tropics is likely due to the removal of small scale unrelated variations, which reduces the standard deviations and leads to an increase in the magnitude of the SHF–SST tendency correlation with the spatial scale.

The transition length scale differs between winter and summer in the WBCs and ARC where there are large SST gradients. In winter, the L_c is around 2.6° (2.2°–3.2°) in the Gulf Stream, and 4.5° (3.9°–5.8°) in the Kuroshio Extension. In summer, the L_c is around 1.3° (0.9°–1.8°) in the Agulhas Return Flow and only 0.9° (0.3°–1.5°) in the Gulf Stream. In the subtropical gyres and the tropics, the atmospheric or oceanic forcing regime is maintained for the examined spatial scales because of the small SST gradients though the magnitude of forcing changes with the spatial scale. The seasonal and regional differences in the transition length scales are related to the pace of decrease of the SST gradient with the spatial smoothing.

The results of the present analysis have implications for the spatial scale dependence of the relationship between ocean and atmosphere in the following aspects. First, it is essential to take into account the spatial scale for the influence of air–sea interaction in the regions where the SST gradients are large. Second, it is important to examine the seasonal difference of change of air–sea relationship with the spatial scale. Third, it is necessary to distinguish the regions for the spatial dependence and seasonal change of air–sea relationship.

The spatial scale dependence of the SST and SHF relationship and its regional feature identified in the present study based on daily data for the mid-latitude regions is consistent with Bishop et al. (2017) and Small et al. (2019) based on monthly data. One new finding of the present study is the difference of the transition length scale between winter and summer. Our analysis based on season stratified data reveals that the transition from the oceanic forcing to the atmospheric forcing in the mid-latitude regions occurs at a smaller spatial scale in summer than in winter. Another finding of the present study is the distinct seasonal change of the air–sea relationship in the Arabian Sea compared to the other tropical regions examined. In particular, in summer, the Arabian Sea region displays features similar to those in the mid-latitude SST frontal zones.

The L_c in the mid-latitude SST frontal regions is 1°–3° based on monthly OAFlux (Bishop et al. 2017) and 4°–7° based on monthly J-OFURO3 (Small et al. 2019). This difference is also obtained in our analysis using the above datasets. Based on the J-OFURO data, the L_c in winter is 3.5° in the Gulf Stream, 5.1° in the Kuroshio Extension, and 3.7° in the ARC and the L_c in summer is 1.5° in the Gulf Stream, 2.3° in the Kuroshio Extension, and 2.3° in the ARC (Table 3). The seasonal difference of the transition length scale between winter and summer and the regional difference of the transition length scale among the three locations

Table 3 Transition length scale in degree at WBCs and ARC in winter and summer based on J-OFURO data

Location	Gulf stream	Kuroshio extension	Agulhas return current
Winter	3.5	5.1	3.7
Summer	1.5	2.3	2.3

agrees with that based on the OAFlux albeit the magnitude is different.

A limitation of this study is that the reasons of why L_c varies from 0.9° to 4.5° in the WBCs and ARC or what determines L_c in regions with large SST gradients are not addressed. Small et al. (2019) mentioned that L_c is related to the atmospheric first baroclinic Rossby radius of deformation, but in their research L_c is between 4° and 7° as using different datasets. Future work is needed to explore the determinant of L_c to contribute to our understanding on spatial scale dependence of air–sea relationship.

Declarations

References

Barsugli JJ, Battisti DS (1998) The basic effects of atmosphere–ocean thermal coupling on midlatitude variability. J Atmos Sci 55:477–493. https://doi.org/10.1175/1520-0469(1998)0552.0.CO;2

Bellucci A, Athanasiadis PJ, Scoccimarro E, Ruggieri P, Gualdi S, Fedele G, Haarsma RJ, Garcia-Serrano J, Castrillo M, Putrahasan D, Sanchez-Gomez E, Moine MP, Roberts CD, Roberts MJ, Seddon J, Vidale PL (2021) Air–sea interaction over the Gulf Stream in an ensemble of HighResMIP present climate simulations. Clim Dyn 56:2093–2111. https://doi.org/10.1007/s00382-020-05573-z

Bishop SP, Small RJ, Bryan FO, Tomas RA (2017) Scale dependence of midlatitude air–sea interaction. J Clim 30:8027–8221. doi:https://doi.org/10.1175/JCLI-D-17-0159.1

Bryan FO, Tomas R, Dennis JM, Chelton DB, Loeb NG, McClean JL (2010) Frontal scale air–sea interaction in high-resolution coupled climate models. J Clim 23:6277–6291. doi:https://doi.org/10.1175/2010JCLI3665.1

Cayan DR (1992) Latent and sensible heat flux anomalies over the northern oceans: driving the sea surface temperature. J Phys Oceanogr 22:859–881. https://doi.org/10.1175/1520-0485(1992)022<0859:LASHFA>2.0.CO;2

Chelton DB, Xie S-P (2010) Coupled ocean–atmosphere interaction at oceanic mesoscales. Oceanography 23:52–69

Chelton DB, Schlax MG, Freilich MH, Milliff RF (2004) Satellite measurements reveal persistent small-scale features in ocean winds. Science 303:978–983. doi:https://doi.org/10.1126/science.1091901

Deser C, Timlin MS (1997) Atmosphere–ocean interaction on weekly timescales in the North Atlantic and Pacific. J Clim 10:393–408. https://doi.org/10.1175/1520-0442(1997)010<0393:AOIOWT>2.0.CO;2

Donohue KA, Watts DR, Hamilton P, Leben R, Kennelly M, Lugo-Fernández A (2016) Gulf of Mexico loop current path variability. Dyn Atmos Oceans 76:174–194. doi:https://doi.org/10.1016/j.dynatmoce.2015.12.003

Duvel JP, Vialard J (2007) Indo-Pacific sea surface temperature perturbations associated with intraseasonal oscillations of tropical convection. J Clim 20:3056–3082. doi:https://doi.org/10.1175/JCLI4144.1

Frankignoul C, Hasselmann K (1977) Stochastic climate models, part II Application to sea-surface temperature anomalies and thermocline variability. Tellus 29:289–305. doi:https://doi.org/10.3402/tellusa.v29i4.11362

Frankignoul C, Czaja A, L'Heveder B (1998) Air–sea feedback in the North Atlantic and surface boundary conditions for ocean models. J Clim 11:2310–2324. https://doi.org/10.1175/1520-0442(1998)011<2310:ASFITN>2.0.CO;2

Fu X, Lee J-Y, Hsu P-C, Taniguchi H, Wang B, Wang W, Weaver S (2013) Multi-model MJO forecasting during DYNAMO/CINDY

period. Clim Dyn 41:1067–1081. doi:https://doi.org/10.1007/s00382-013-1859-9

Hasselmann K (1976) Stochastic climate models Part I. Theory Tellus 28:473–485. doi:https://doi.org/10.3402/tellusa.v28i6.11316

Jing Z et al (2020) Maintenance of mid-latitude oceanic fronts by mesoscale eddies. Sci Adv 6:eaba7880. doi:https://doi.org/10.1126/sciadv.aba7880

Jouanno J, Ochoa J, Pallàs-Sanz E, Sheinbaum J, Andrade-Canto F, Candela J, Molines J-M (2016) Loop current frontal eddies: formation along the Campeche Bank and impact of coastally trapped waves. J Phys Oceanogr 46:3339–3363. https://doi.org/10.1175/JPO-D-16-0052.1

Kirtman BP et al (2012) Impact of ocean model resolution on CCSM climate simulations. Clim Dyn 39:1303–1328. doi:https://doi.org/10.1007/s00382-012-1500-3

Kitoh A, Arakawa O (1999) On overestimation of tropical precipitation by an atmospheric GCM with prescribed SST. Geophys Res Lett 26:2965–2968. doi:https://doi.org/10.1029/1999gl900616

Kushnir Y, Held IM (1996) Equilibrium atmospheric response to North Atlantic SST anomalies. J Clim 9:1208–1220. https://doi.org/10.1175/1520-0442(1996)009<1208:EARTNA>2.0.CO;2

Manabe S, Stouffer RJ (1996) Low-frequency variability of surface air temperature in a 1000-year integration of a coupled atmosphere–ocean–land surface model. J Clim 9:376–393. https://doi.org/10.1175/1520-0442(1996)009<0376:LFVOSA>2.0.CO;2

Putrasahan DA, Miller AJ, Seo H (2013) Isolating mesoscale coupled ocean–atmosphere interactions in the Kuroshio Extension region. Dyn Atmos Oceans 63:60–78. doi:https://doi.org/10.1016/j.dynatmoce.2013.04.001

Putrasahan DA, Kamenkovich I, Le Hénaff M, Kirtman BP (2017) Importance of ocean mesoscale variability for air–sea interactions in the Gulf of Mexico. Geophys Res Lett 44:6352–6362. https://doi.org/10.1002/2017GL072884

Reynolds RW, Smith TM, Liu C, Chelton DB, Casey KS, Schlax MG (2007) Daily high-resolution-blended analyses for sea surface temperature. J Clim 20:5473–5496. doi:https://doi.org/10.1175/2007JCLI1824.1

Schott FA, McCreary JP Jr (2001) The monsoon circulation of the Indian Ocean. Progress Oceanogr 51:1–123. https://doi.org/10.1016/S0079-6611(01)00083-0

Small RJ et al (2008) Air–sea interaction over ocean fronts and eddies. Dyn Atmos Oceans 45:274–319. doi:https://doi.org/10.1016/j.dynatmoce.2008.01.001

Small RJ, Bryan FO, Bishop SP, Tomas RA (2019) Air–sea turbulent heat fluxes in climate models and observational analyses: what drives their variability? J Clim 32:2397–2421. https://doi.org/10.1175/JCLI-D-18-0576.1

Storch V (2000) Signatures of air–sea interactions in a coupled atmosphere–ocean GCM. J Clim 13:3361–3379. https://doi.org/10.1175/1520-0442(2000)013<3361:SOASII>2.0.CO;2

Sun X, Wu R (2021) Seasonality and time scale dependence of the relationship between turbulent surface heat flux and SST. Clim Dyn:online. https://doi.org/10.1007/s00382-021-05631-0

Trenberth KE, Shea DJ (2005) Relationships between precipitation and surface temperature. Geophys Res Lett 32:L14703. https://doi.org/10.1029/2005gl022760

Wallace JM, Smith C, Jiang Q (1990) Spatial patterns of atmosphere-ocean interaction in the northern winter. J Clim 3:990–998. https://doi.org/10.1175/1520-0442(1990)003<0990:SPOAOI>2.0.CO;2

Wang B, Ding Q, Fu X, Kang I-S, Jin K, Shukla J, Doblas-Reyes F (2005) Fundamental challenge in simulation and prediction of summer monsoon rainfall. Geophys Res Lett 32:L15711. https://doi.org/10.1029/2005gl022734

Wu R (2016) Coupled intraseasonal variations in the East Asian winter monsoon and the South China Sea–western North Pacific SST in boreal winter. Clim Dyn 47:2039–2057. https://doi.org/10.1007/s00382-015-2949-7

Wu R (2019) Summer precipitation–SST relationship on different time scales in the northern tropical Indian Ocean and western Pacific. Clim Dyn 52:5911–5926. https://doi.org/10.1007/s00382-018-4487-6

Wu R, Chen Z (2015) Intraseasonal SST variations in the South China Sea during boreal winter and impacts of the East Asian winter monsoon. J Geophys Res Atmos 120:5863–5878. https://doi.org/10.1002/2015jd023368

Wu R, Kinter JL III (2010) Atmosphere-ocean relationship in the mid-latitude North Pacific: seasonal dependence and east-west contrast. J Geophys Res 115:D06101. https://doi.org/10.1029/2009jd012579

Wu R, Kirtman BP (2004) Impacts of the Indian Ocean on the Indian summer monsoon–ENSO relationship. J Clim 17:3037–3054. https://doi.org/10.1175/1520-0442(2004)017<3037:IOTIOO>2.0.CO;2

Wu R, Kirtman BP (2005) Roles of Indian and Pacific Ocean air–sea coupling in tropical atmospheric variability. Clim Dyn 25:155–170. https://doi.org/10.1007/s00382-005-0003-x

Wu R, Kirtman BP (2007) Regimes of seasonal air–sea interaction and implications for performance of forced simulations. Clim Dyn 29:393–410. https://doi.org/10.1007/s00382-007-0246-9

Wu R, You T (2018) Summer intraseasonal surface heat flux–sea surface temperature relationship over Northern Tropical Indo-Western Pacific in climate models. J Geophys Res Atmos 123:5859–5880. https://doi.org/10.1029/2018jd028468

Wu R, Kirtman BP, Pegion K (2006) Local air–sea relationship in observations and model simulations. J Clim 19:4914–4932. https://doi.org/10.1175/JCLI3904.1

Wu R, Kirtman BP, Pegion K (2007) Surface latent heat flux and its relationship with sea surface temperature in the National Centers for Environmental Prediction Climate Forecast System simulations and retrospective forecasts. Geophys Res Lett 34:L17712. https://doi.org/10.1029/2007gl030751

Wu R, Cao X, Chen S (2015) Covariations of SST and surface heat flux on 10–20 day and 30–60 day time scales over the South China Sea and western North Pacific. J Geophys Res Atmos 120:12486–12499. https://doi.org/10.1002/2015jd024199

Yu L, Weller RA (2007) Objectively analyzed air–sea heat fluxes for the global ice-free oceans (1981–2005). Bull Am Meteorol Soc 88:527–540. https://doi.org/10.1175/BAMS-88-4-527